

Grain-Boundary-Activity Correlation for Electrocatalytic Oxygen Evolution in High-Entropy Alloys

Tao Zhang^{①,‡}, Niu Gao,^{2,‡} Zheng-Jie Chen,³ Hui-Feng Zhao^①, Ya-Song Wang^②, Jun-Qing Yao,² Jing Peng^③, Yuan-Miao Sun^③, Hai-Bin Yu^{①,*}, and Xin-Wang Liu^{②,†}

¹ Wuhan National High Magnetic Field Center and School of Physics, Huazhong University of Science and Technology, Wuhan 430074, China

² State Key Laboratory of Materials Processing and Die and Mould Technology, School of Materials Science and Engineering, Huazhong University of Science and Technology, Wuhan 430074, China

³ Shenzhen Key Laboratory of Energy Materials for Carbon Neutrality, Shenzhen Institute of Advanced Technology, Chinese Academy of Sciences, Shenzhen 518055, China

(Received 5 June 2023; revised 14 July 2023; accepted 21 July 2023; published 22 August 2023)

High-entropy alloys (HEAs) have emerged as a promising platform for designing efficient electrocatalysts; however, the relationship between their structure and activity has not yet been clearly established. In particular, the influences of crystalline defects, such as grain boundaries (GBs), on activity and stability remain unclear. This study demonstrates the impacts of GBs on the oxygen evolution reaction (OER) activity in the FeCoCrNi HEA. We observe a logarithmic dependence of OER performance on mean grain size, spanning 3 orders of magnitude, as measured by evaluators like overpotential and Tafel slope. Spatially resolved microscopic imaging of activated samples indicates that the GBs undergo substantial reconstructions and they are enriched with the *in situ* formed metal oxides (M-O, M = Fe, Co, Ni) and the amorphous regions. By comparing with simple metals, we reveal a “high-entropy effect,” i.e., HEAs exhibit greater tolerance towards the grain refinements, which explains their activity both in bulk samples and nanoparticles. These findings offer physics-informed strategies for developing HEA electrocatalysis.

DOI: 10.1103/PRXEnergy.2.033011

I. INTRODUCTION

Electrochemical energy conversion is essential for achieving clean energy storage, and the oxygen evolution reaction (OER) is usually a critical rate-determining process in a variety of energy technologies, including water splitting, metal-air batteries, and carbon dioxide reduction [1–4]. The slow kinetics of OER pose a significant bottleneck for these applications, highlighting the urgent need for low-cost and high-efficient catalyst electrodes [5–9].

Recently, high-entropy materials, especially high-entropy alloys (HEAs), have garnered significant attention as a promising platform for new catalyst design [10–20]. HEAs are composition complex alloys, comprising at least four components in equal or nearly equal atomic

ratios [21,22]. The random distribution of atoms in HEAs provides a large number of binding sites for intermediates for catalytic reaction, leading to a nearly continuous adsorption energy distribution [23].

Although there has been increasing interest in HEAs as electrocatalysts for the OER, the mechanism that makes them exceptional remains unclear, and the structure-activity relationship is yet to be fully established. Certain studies suggest that HEAs may act as precursor materials for the OER, as surface restructuring and even amorphization have been observed in activated samples [12,24,25]. As a result, it is crucial to investigate the reconstruction process [26–29].

In this regard, intrinsic defects such as grain boundaries (GBs), vacancies, and dislocations are of considerable relevance. These topics have been demonstrated for mechanical properties [30], but are less studied for electrocatalysis in HEAs. They could contribute in at least three ways. Firstly, defects may provide localization for the initialization of surface reconstruction. Secondly, defects themselves may act as effective activation sites for OER due to their structure and composition perturbations. Thirdly, defects could impact the transport processes of reactions, modifying the pathway and speed of reactant

*habinyu@hust.edu.cn

†liuxw@hust.edu.cn

‡These authors contributed equally.

transportation. As a result, they have the potential to regulate the overall kinetics of electrocatalytic reactions.

Scrutinizing the role of defects in the OER can offer insight into the origin of restructuring and the structure-activity relationship in HEAs, providing an additional degree of freedom for the development of HEA-based catalysts.

Grain boundaries are the most common structure in polycrystalline materials; they create strained regions with atomic packing that differs from the grain interiors [31,32]. They have higher energy and entropy than other defects such as twinning and dislocations. In some previous work, the role of GBs on electrocatalysis has been demonstrated in CO₂ reduction reactions in a pure metal like Cu and Au [33–35].

However, separating the role of GBs from other factors in HEAs is particularly challenging compared to pure metals and simple alloys, because most of the as-prepared HEAs are in a thermodynamically metastable state and exhibit subtle chemical short-range orders that are sensitive to sample history. Different preparation methods can result in variations in chemical short-range order and other types of defects, such as vacancies and dislocations, or even induce chemical inhomogeneity [36,37]. As a result, devising a consistent method for varying grain sizes in HEAs is crucial.

To address these challenges, we employed a cold rolling-recrystallization technique to systematically adjust the grain sizes of a typical FeCoCrNi HEA while maintaining other factors nearly constant. By doing so, we obtained samples with varying grain sizes and observed that the OER activity followed a logarithmic dependence

on the mean grain size in both the HEAs and simple alloys. Notably, HEAs displayed a weaker dependence on GB density than simple alloys, which explains their exceptional performance even in bulk materials.

We also demonstrate that GBs play a crucial role in the reconstruction process during the OER, which is the primary source of the active phase. Our analysis of the OER process using a molecule probe and *in situ* Raman spectroscopy showed that high GB density samples have more OER-active intermediates covering their surfaces.

II. RESULTS

A. Characterization of grain boundaries

As depicted in Fig. 1(a), we obtain bulk samples with varying grain sizes through cold rolling and subsequent recrystallization anneals [38,39]. This process transforms the columnar grains of the as-cast HEAs into equiaxed grains, resulting in chemical composition homogeneity. Prior to cold rolling, a homogenization annealing at 1473 K for 12 h was performed. The cold rolling leads to a thickness reduction of 85%. Subsequently, by varying the recrystallization conditions (temperature and time, Table I), we can produce average grain sizes ranging from 0.8 to 300 μm, spanning nearly 3 orders of magnitude.

Control samples (FeCoNi, FeNi, and Ni) with differently sized grains were also prepared using the same method (see Figs. S2–S4 within the Supplemental Material [40] for structural information of the samples). These control samples were used to compare with the HEAs, because they all have common elements with the HEA and similar face-center-cubic (fcc) structures. Table I lists the

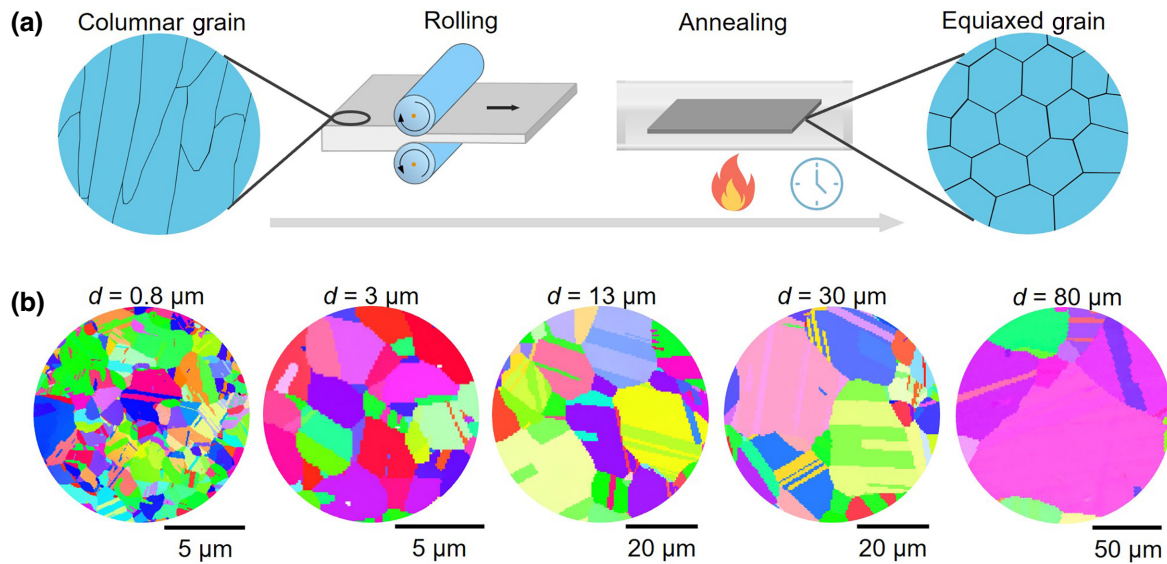


FIG. 1. Grain refinement process. (a) Scheme of thermomechanical processing. (b) Electron backscatter diffraction microstructures of the FeCoCrNi HEAs after different recrystallization anneals, resulting in equiaxed grains with various mean grain sizes.

TABLE I. List of sample recrystallization conditions (annealing temperature T_A and time t_A), mean grain size (d), and OER evaluators (overpotential η at 10 mA/cm² and corresponding Tafel slope).

Sample	T_A (K)	t_A (min)	d (μm)	η (mV)	Tafel slope (mV dec ⁻¹)
FeCoCrNi	973	10	0.8	259	36.7
	973	30	1.2	263	38.6
	1073	10	2	270	41.1
	1073	30	3	276	42.1
	1073	1500	7	286	44.3
	1123	1500	13	294	46.2
	1223	1500	30	308	50.3
	1323	6000	80	325	53.6
	1473	2880	180	335	58.6
	1523 ^a	2880	300	359	65.6
FeCoNi	973	10	5	295	42.3
	1073	30	10	306	46.1
	1123	1500	15	318	49.6
	1173	1500	25	328	51.4
	1223	1500	30	333	52
	1473	2880	255	363	66.4
FeNi	973	10	5	310	42.4
	1073	10	13	324	46.3
	1073	30	17	336	51.1
	1123	1500	20	340	51.7
	1223	1500	50	354	55.9
	1473	2880	260	380	66.8
Ni	973	10	35	372	57.9
	1073	30	45	378	59.1
	1123	1500	57	380	61.8
	1073	1500	73	385	62.4
	1223	1500	93	391	65.6
	1473	2880	180	404	68.6

^aAnnealing without cold rolling.

recrystallization conditions and resulting sample properties. We note that adding Cr, Fe, and Co to Ni metal can lead to changes in the stacking fault energy, affecting the recrystallization process. Therefore, under the same annealing conditions, the grain size formed by each system is different, and the HEAs reach the smallest grain size.

The microstructure and GB characteristics of the FeCoCrNi HEA are indexed by electron backscatter diffraction. As a typical example, Fig. 1(b) shows the inverse pole figures (IPFs) of the FeCoCrNi HEA with different average grain sizes. They all show equiaxed grains containing profuse $\Sigma 3$ annealing twins because of the low stacking fault energy. The IPFs also show that the texture is almost random, with only a fragile residual texture. The slight texture obtained after cold deformation and recrystallization are typical in fcc metals and alloys, which also occurs in previous work [41,42]. Moreover, the densities of annealing twins and twin boundaries are quite similar in all samples (Fig. S1 within the Supplemental Material [40]).

This indicates that the GB characteristics (including large- and low-angle GBs, twin boundaries) of each annealed sample do not differ significantly and only the grain size varies. Additional characterizations by x-ray diffraction and transmission electron microscopy (TEM) show that the samples are composed of a single fcc phase and with homogeneous chemical composition distribution at GBs (Figs. S5–S7 within the Supplemental Material [40]).

In short, the FeCoCrNi HEAs investigated here are single-phase fcc solid solutions having equiaxed nearly random grains and similar types of GBs. Their average grain size can be tuned by thermal-mechanical processing. These samples offer us the opportunity to study the relationship between grain size and OER performance.

B. Relation between grain size and OER performance

The OER activity of FeCoCrNi HEAs and the control samples (FeCoNi, FeNi, and Ni) with different grain sizes were evaluated in a 1-mole/L KOH electrolyte using a standard three-electrode system. Details about the electrocatalysis measurements are presented in the Supplemental Material, which contains the linear sweep voltammetry (LSV) and cyclic voltammetry curves, Nyquist plots, and the estimated double-layer capacitance for each sample (see Figs. S8–S14 within the Supplemental Material [40]). Moreover, the normalized electrocatalytic performance of electrochemical active surface area of different grain sizes also revealed that fine-grained samples presented better catalytic activity than the other contents [43,44] (Figs. S15–S17 within the Supplemental Material [40]). Here we focus on the main results in Fig. 2.

We find that both the overpotential and Tafel slope exhibit a clear dependence on grain size for all the samples. For example, the overpotential required to reach a current density of 10 mA/cm² varies from 259 mV for $d = 0.8 \mu\text{m}$ to 359 mV for $d = 300 \mu\text{m}$ for the FeCoCrNi HEA. This indicates higher reactivity for samples with fine grain sizes. This is consistent with a previous report that also showed that HEA with fine grain size has better OER performance [45]. All the control samples show the same general feature.

Meanwhile, at the same grain size, the overpotential is notably smaller for the HEA than for control samples. This indicates that HEAs are more intrinsically active. Interestingly, both overpotential (η) and Tafel slopes (s) show a logarithmic dependence on the grain size (d in micrometers):

$$\eta = A_\eta + B_\eta \times \log_{10}(d), \quad (1)$$

$$s = A_s + B_s \times \log_{10}(d), \quad (2)$$

with A and B fitting parameters. Physically, slope B characterizes how OER properties are dependent on the grain

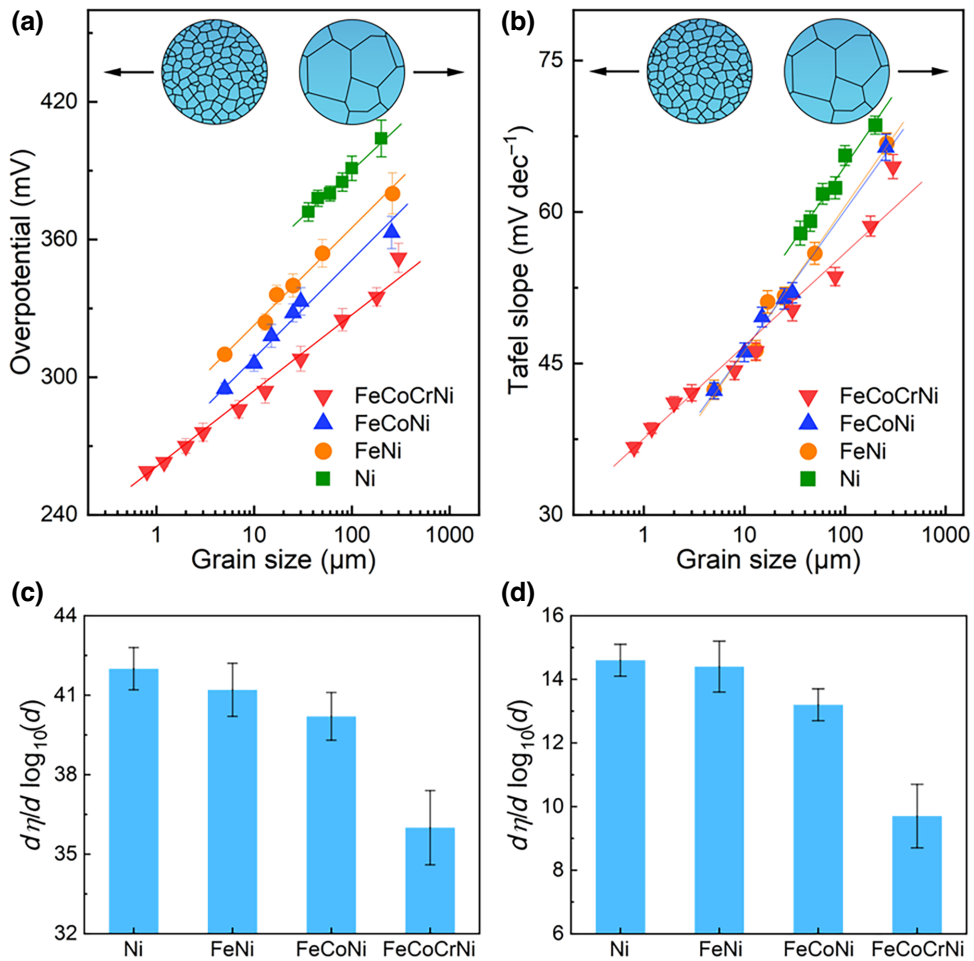


FIG. 2. Relationship between electrocatalytic OER performance and grain size. Plots of overpotential (a) and Tafel slope (b) versus $\log(d)$. The $d\eta/d \log_{10}(d)$ (d) and $ds/d \log_{10}(d)$ (e) values of Ni, FeNi, FeCoNi, and FeCoCrNi systems.

size variation. For example, if B is a large positive value, the η would decrease substantially with grain refinements. On the other hand, if $B = 0$, η would be insensitive to the GBs.

The slope values of B_η and B_s for different systems are compared in Figs. 2(c) and 2(d), respectively. We find that B is decreasing from low- to high-entropy materials. The FeCoCrNi HEA has considerably smaller B than other control samples. This reveals a high-entropy effect and implies that the HEAs are more tolerant to the grain size of the samples. Actually, some recent experiments have shown that the bulk HEA exhibits good activity [12]. This would facilitate material design and industry-scale applications.

C. Reconstructions around grain boundaries after OER

We characterized the surface of samples after OER and found direct indications of higher OER activity at GBs. As a typical example, Fig. 3(a) shows the SEM images of an

HEA sample with $d = 30 \mu\text{m}$, which reveals a dense distribution of oxides along GBs. In contrast, only a small amount of oxides are present in the grain interiors. Thus, the real catalytic function in OER might be at the reconstructed structure of the surface, and they are enriched on the GBs (Fig. S18 within the Supplemental Material [40]). This represents a piece of structural evidence for the correlation between the GB and activity, as presented above.

Figure 3(c) show the TEM image of the fine structure of the HEA sample after electrochemical activation. Specifically, the TEM specimen was first prepared (and observed by TEM), and then tested in the 1-mole/L KOH with 1.5 V for 5 s and reexamined by TEM. Figure 3(c) shows that there are obvious crazelike structures of the electrochemically corroded GBs. The insets of Fig. 3(c) show the two diffraction patterns at the right and left sides of the corroded GB. They show that the two parts have different lattice orientations. Thus, the corroded GBs are confirmed to be at the interface of two different grains.

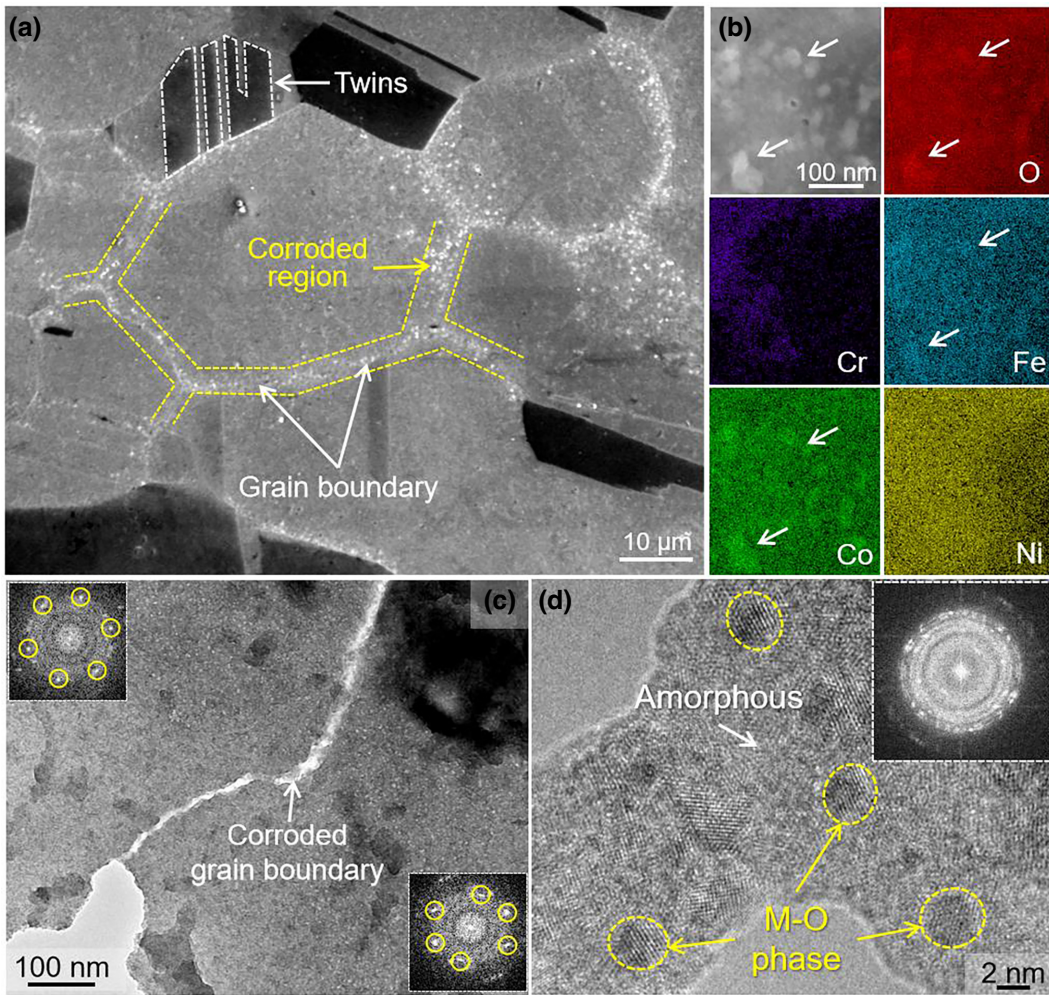


FIG. 3. Microstructures of the activated HEA sample. (a) SEM image: the M-O phases enriched at GBs are marked with yellow dashed lines. The twins or twin boundaries are marked with white dashed lines. (b) Elemental maps of O, Cr, Fe, Co and Ni in the region containing oxide particles. (c) HRTEM image at the grain boundary with FFT patterns of the left and right grains inserted. (d) Enlarged view of the red box in (c). The M-O phases enriched at GBs are marked with yellow circles.

Moreover, the HRTEM image of Fig. 3(d) indicates that the structure at GBs after electrochemical activation is disordered and tends to be amorphous. It is thus a composite of amorphous regions and the HEA crystalline matrix covering the polycrystalline M-O phase. This order-disorder structure has been reported in previous studies, which suggests that it combines high OER activity and good electrical conductivity for electron transportation [46]. Meanwhile, some previous works have illustrated that amorphous alloys or metallic glasses have better activity than their crystalline counterparts [47,48].

Technically, we were caution to verify that the corroded GB and the amorphous regions were not caused by the preparation process of the TEM sample. The TEM samples were prepared by the twin-jet electron chemical thinning technique at a low temperature of 253 K. Furthermore,

HRTEM observations at the grain boundaries revealed that the integrity of the GBs was maintained and unaffected by the preparation technique for the samples that were not electrochemically activated (Fig. S7b within the Supplemental Material [40]).

The elemental maps in Fig. 3(b) show that the signals of Fe, Co, Ni, and O remain strong on the oxidized surface, while Cr is severely depleted. The oxide particles are due to aggregations and they are essentially a multimetal oxide M-O ($M = \text{Fe}, \text{Co}, \text{Ni}$). In addition, the inductively coupled plasma optical emission spectrometer (ICP-OES) results show the presence of more Cr and Fe ions in the electrolyte solution after OER, while the contents of Co and Ni are low (Fig. S19 within the Supplemental Material [40]). These results indicate that the surface metal elements at the GBs are leached in the reconstruction process, especially Cr. Leaching of Cr and Fe will further intensify the

surface reconstruction of the catalyst, which can promote effective bulk charge transfer and improve conductivity during the OER process.

Overall, these findings indicate that the GBs are easier to reconstruct during the OER activation than the interior grains.

D. Surface states of the HEA after activation

We used XPS to analyze the electronic structure of activated HEA samples (after the OER activation) with different grain sizes and obtained the valence state information of each element at the reacted surfaces. XPS survey spectra show that Fe, Co, and Ni are present on the surfaces of all the samples (Fig. S20a within the Supplemental Material [40]).

Figure 4(a) presents the high-resolution XPS spectrum of Fe $2p$, which includes two spin orbitals. Taking the HEA sample with $d = 0.8 \mu\text{m}$ as a typical example, the analysis suggests that the peaks at binding energies of 711.2, 716.3, and 726.3 eV can be assigned to $\text{Fe}^{3+} 2p_{3/2}$, a satellite peak, and $\text{Fe}^{3+} 2p_{1/2}$, respectively.

Notably, compared with other samples of larger grain size, the $\text{Fe}^{3+} 2p_{1/2}$ of the HEA with smaller grain size shows a higher oxidation state. This suggests that samples with smaller d have a strong binding tendency with oxygen [49].

Regarding the fitting of the XPS spectrum of Ni $2p$ [Fig. 4(b)], the peaks observed at 856.2, 856.6, and 882 eV can be assigned to Ni^{2+} , Ni^{3+} , and a satellite peak, respectively [50,51]. The position of the $\text{Ni}^{3+} 2p_{3/2}$ peak of the $d = 0.8 \mu\text{m}$ sample is shifted about 0.38 eV towards a higher binding energy compared with the sample with the largest grain size. Thus, Ni and Fe show a similar trend.

We attribute these above features to the greater density of GBs in the samples with smaller d , which amplifies the contribution of Fe and Ni electronic states at GBs.

For Co $2p$, as shown in Fig. 4(c), XPS results did not reveal a discernible difference in the binding energy of Co^{3+} for samples with various grain sizes, indicating a

similar Co oxidation state across these samples. The higher valence metals (Fe^{3+} , Ni^{3+} , Co^{3+}) can increase the adsorption capacity of OH and thus accelerate the OER [52,53]. Moreover, Cr $2p$ was detected with a low signal, indicating that Cr was much leached as a sacrificial element during the surface reconstruction (Fig. S20b within the Supplemental Material [40]). In addition, comparing the XPS results of Ni, Fe, and Co reveals that the effect of Cr on the electronic configuration of other elements is weak, which is closely related to the mass leaching of Cr (Fig. S21 within the Supplemental Material [40]). The analysis of O $1s$ shows that the binding of metal elements and O is mainly present on the sample surface as M-OH species (Fig. S20c within the Supplemental Material [40]).

E. Detecting intermediates

The dependence of the OER activity of FeCoCrNi on the grain size is mainly reflected in the GB density. Therefore, we expect that the change in GB density will directly cause the difference in reaction intermediates in the OER process. Previous reports [54] have shown that alcohol molecules behaving as nucleophilic reagents readily react with the electrophilic OH^* adsorbed on the surface of OER electrodes. In this way, the anodic oxidation in a mixed electrolyte of methanol and KOH exhibits a competition between the methanol oxidation reaction (MOR) and OER for OH^* . This is advantageous for the detection of OH^* , the first intermediate in the OER process.

We performed methanol oxidation tests using the difference in reaction kinetics between alcohol molecular oxidation and OER. As shown in Figs. 5(a) and 5(d), the increase in MOR current density with increasing voltage is more sensitive for HEA $d = 0.8 \mu\text{m}$ than ones with larger d , indicating that more OH^* is adsorbed on the surface of a fine-grained sample. The differences in catalyst surfaces mainly arise from the different GB densities and their reconstructions. Thus, they enrich the adsorption of intermediates in the OER process.

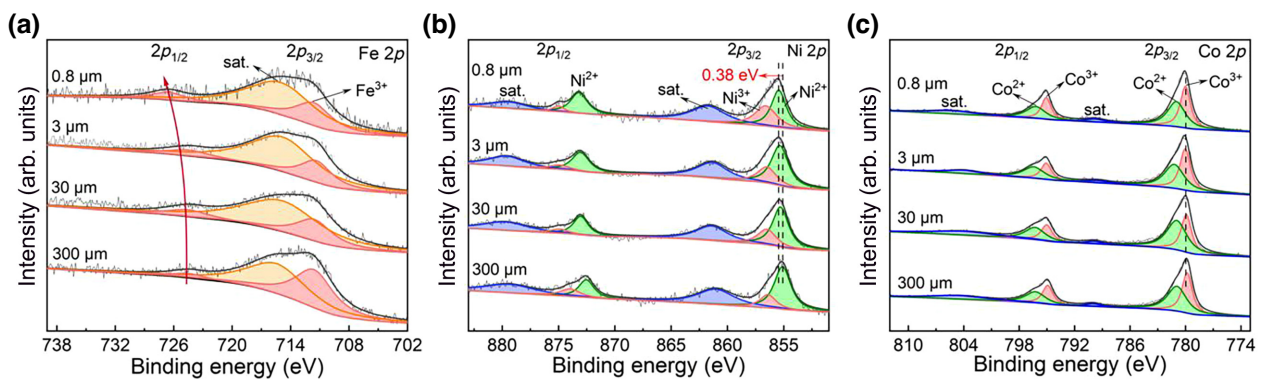


FIG. 4. XPS spectra for HEA samples with $d = 0.8, 3, 30$, and $300 \mu\text{m}$: (a) Fe $2p$, (b) Ni $2p$, and (c) Co $2p$.

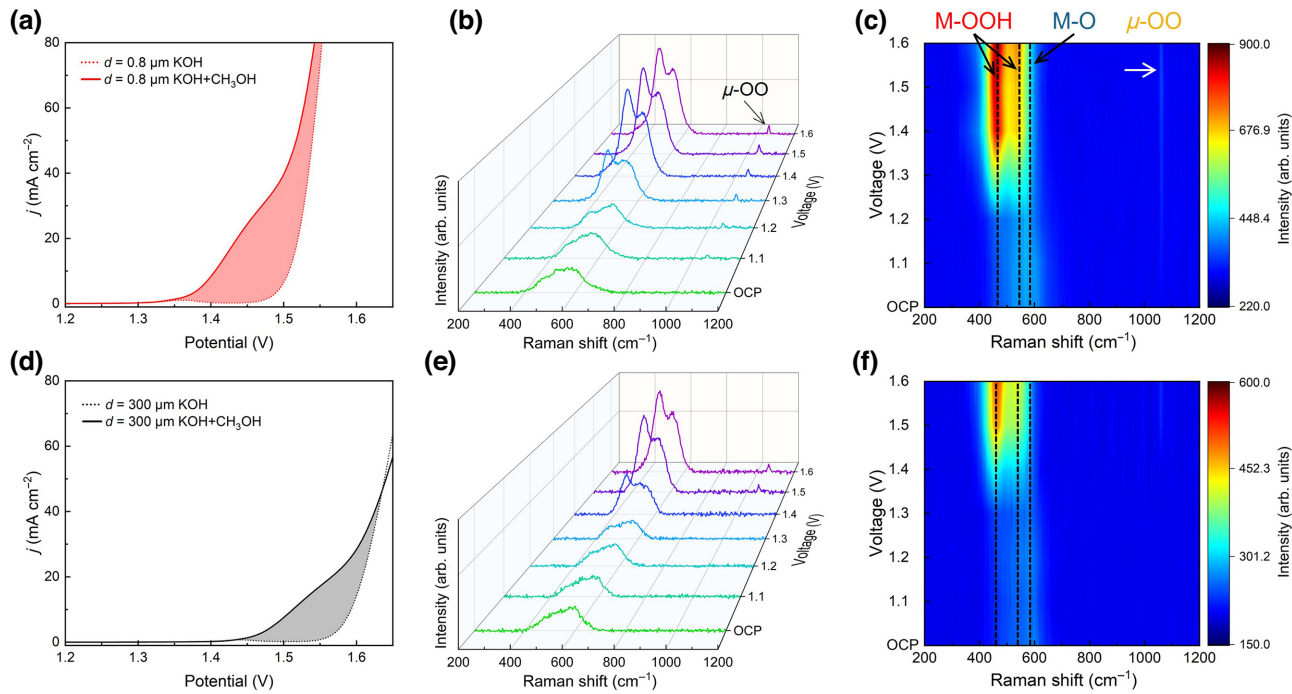


FIG. 5. Origin of electrochemical activity in the OER process. LSV curves of (a) $d = 0.8 \mu\text{m}$ and (d) $d = 300 \mu\text{m}$ in 1.0-mole/L KOH with and without methanol. *In situ* Raman spectroscopy measurements of $d = 0.8 \mu\text{m}$ (b),(c) and $d = 300 \mu\text{m}$ (e),(f) at different reaction voltages.

We conducted *in situ* Raman spectroscopy to detect OER-intermediate species on the surface of two typical samples with different d . As shown in Figs. 5(b) and 5(c), the Raman spectra of the HEA $d = 0.8\text{-}\mu\text{m}$ sample at open circuit potential and low voltage [< 1.3 V versus reversible hydrogen electrode (RHE)] show a weak band. The Raman peak at 589 cm^{-1} can be assigned to the stretching vibration of M-O in M-OH, where M might be Co or Ni. With increasing voltage (> 1.3 V versus RHE), the Raman spectra show two well-defined peaks at 472 and 552 cm^{-1} , which can be assigned to the bending and stretching modes of M-O in M-OOH, respectively. Thus, the formation of -OOH is a key intermediate, indicating the transformation from M-OH to M-OOH and the source of high activity [50].

We note that, although the Raman results show a preference for the formation of NiOOH, the Raman signals of the Co—O bond in CoOOH and the Ni—O bond in NiOOH may override each other; therefore, the exact role of each element in the OER process cannot be uniquely determined [55]. Nevertheless, the results clearly support the claim that oxidation of M-OH on the FeCoCrNi surface is accomplished through a hydroxide-mediated deprotonation process, which is consistent with previous reports [56,57].

As compared to the fine-grained samples, the peaks of M-O (both in M-OH and M-OOH) in the Raman spectra of the HEA $d = 300\text{-}\mu\text{m}$ samples exhibit lower intensities, as shown in Figs. 5(e) and 5(f). We note that this variation

is over the entire applied voltage range, which implies that the reconstructed surface with small grain size has more reaction intermediate involved in the OER process, and thus has higher activity.

Also of particular interest is the effect of grain size on the Raman peak of the superoxide species at 1069 cm^{-1} , which is another kind of active intermediate $\mu\text{-OO}$ of the OER process identified in previous reports [58,59]. On the other hand, the $\mu\text{-OO}$ can hardly be detected in the sample with $d = 300 \mu\text{m}$.

Thus, *in situ* Raman spectroscopy demonstrates that HEAs with abundant GBs have a higher degree of coverage by intermediates in the OER process. This is in agreement with the results of alcohol molecules probing OER intermediates. Both findings indicate that the reconstructed GBs bear the main source of activity, and samples with a high density of reconstructed GBs carry more active species.

III. DISCUSSION

Based on the above experimental findings, a preliminary understanding of the GB and activity might be surmised. The GBs are precursor regions where the reconstruction initiates and progressively expands towards the grain interiors. These regions contain the real active species for the OER.

We suggest a simplified thermodynamic consideration to interpret why the activity is dependent on the mean

grain size in a logarithmic manner. We consider the number of “effective active sites” N to be stochastic along with the reconstructed GB regions, and the number density along the length (l) of the GBs, dN/dl , is proportional to the chemical potential difference $\delta\mu \propto -2\sigma/l$, where σ is the surface energy per area, and one might write $dN/dl \propto \delta\mu \propto -\sigma/l$. This assumes that a shorter l is higher in the density of effective active sites. One can obtain $N \propto -\log(l)$, which is consistent with the experimentally determined Eq. (1). This suggests that $\delta\mu$ is an important factor in promoting the activity. Furthermore, since $\delta\mu$ is related to the Gibbs free energy that comprises the entropy item ($-TS$), the HEA with larger mixing entropy ΔS_{mix} would be more pronounced in lowering this value. This further explains why the B values in Eqs. (1) and (2) are smaller in HEAs compared to simple metals. Fundamentally, the reason behind this lies in the increased number of configurations that grain boundaries can offer.

In addition, our results also indicate that twins and twin boundaries are not predominant factors in OER in HEAs. As seen in Fig. 3(a), the twin boundaries did not experience as much oxidation and restructuring as the GBs. This might be explained by the fact that the twin boundaries are predominately coherent and not as defective as GBs. Typically, they have low interfacial energy, approximately 1/10 of the GBs [60].

Our results have direct implications for the design of materials used in OER. For instance, currently, most of the studied electrocatalysts are nanomaterials with small grain sizes, resulting in numerous structural defects and a large electrochemical active surface area. On the other hand, bulk materials generally exhibit better stability and can serve as integrated electrodes; however, they sacrifice surface area. Given that grain boundaries are recognized as crucial regions for OER and reconstructions, there is an inclination to develop bulk high-entropy alloys with nanosize grains or employ surface nanostructuring [61]. It would be possible to combine the advantages of both approaches into a single material.

IV. CONCLUSION

We have shown that increasing the GB density can enhance the OER activity in a family of metals, including HEA FeCoCrNi, FeCoNi, FeNi, and Ni. Grain boundaries are the main source of catalytic activity. In particular, we have established a linear relationship between the OER performance and the logarithm of the grain size and observed that the reconstructed GBs in the FeCoCrNi HEA are a crystalline-amorphous structure loaded with more metal oxides. According to the results of MOR and *in situ* Raman spectroscopy, the active species for OER include M-OOH and μ -OO, and the fine-grained HEA surface adsorbs more active intermediates during OER. Compared with simple alloys, OER activity on HEAs shows relatively

milder dependence on GBs. Our findings also suggest that defect engineering through grain refinement can be applied to other alloy systems to improve their electrocatalytic OER performance.

ACKNOWLEDGMENTS

The work at HUST was supported by the National Thousand Young Talents Program of China and the Fundamental Research Funds for Central Universities (2018KFYXKJC009). We thank Professor Zhao-Ping Luo (Institute of Metal Research, Chinese Academy of Sciences) and Professor Ran Li (Beihang University) for helpful discussions and material fabrications.

- [1] Z. W. Seh, J. Kibsgaard, C. F. Dickens, I. B. Chorkendorff, J. K. Norskov, and T. F. Jaramillo, Combining theory and experiment in electrocatalysis: Insights into materials design, *Science* **355**, eaad4998 (2017).
- [2] X. Liu, J. Meng, J. Zhu, M. Huang, B. Wen, R. Guo, and L. Mai, Comprehensive understandings into complete reconstruction of precatalysts: Synthesis, applications, and characterizations, *Adv. Mater.* **33**, e2007344 (2021).
- [3] B. Zhang *et al.*, Homogeneously dispersed multimetal oxygen-evolving catalysts, *Science* **352**, 333 (2016).
- [4] Y. Shi and B. Zhang, Recent advances in transition metal phosphide nanomaterials: Synthesis and applications in hydrogen evolution reaction, *Chem. Soc. Rev.* **45**, 1529 (2016).
- [5] Y. C. Yao *et al.*, Engineering the electronic structure of single atom Ru sites via compressive strain boosts acidic water oxidation electrocatalysis, *Nat. Catal.* **2**, 304 (2019).
- [6] N. Zhang, X. Feng, D. Rao, X. Deng, L. Cai, B. Qiu, R. Long, Y. Xiong, Y. Lu, and Y. Chai, Lattice oxygen activation enabled by high-valence metal sites for enhanced water oxidation, *Nat. Commun.* **11**, 4066 (2020).
- [7] F. Qin, Z. H. Zhao, M. K. Alam, Y. Ni, F. Robles-Hernandez, L. Yu, S. Chen, Z. F. Ren, Z. M. Wang, and J. M. Bao, Trimetallic NiFeMo for overall electrochemical water splitting with a low cell voltage, *ACS Energy Lett.* **3**, 546 (2018).
- [8] S. Dresp, F. Luo, R. Schmack, S. Kühl, M. Gleich, and P. Strasser, An efficient bifunctional two-component catalyst for oxygen reduction and oxygen evolution in reversible fuel cells, electrolyzers and rechargeable air electrodes, *Energy Environ. Sci.* **9**, 2020 (2016).
- [9] Z. J. Wang, M. X. Li, J. H. Yu, X. B. Ge, Y. H. Liu, and W. H. Wang, Low-iridium-content IrNiTa metallic glass films as intrinsically active catalysts for hydrogen evolution reaction, *Adv. Mater.* **32**, e1906384 (2020).
- [10] T. A. A. Batchelor, J. K. Pedersen, S. H. Winther, I. E. Castelli, K. W. Jacobsen, and J. Rossmeisl, High-entropy alloys as a discovery platform for electrocatalysis, *Joule* **3**, 834 (2019).
- [11] T. Löffler, A. Savan, A. Garzón-Manjón, M. Meischein, C. Scheu, A. Ludwig, and W. Schuhmann, Toward a

- paradigm shift in electrocatalysis using complex solid solution nanoparticles, *ACS Energy Lett.* **4**, 1206 (2019).
- [12] Z. J. Chen, T. Zhang, X. Y. Gao, Y. J. Huang, X. H. Qin, Y. F. Wang, K. Zhao, X. Peng, C. Zhang, L. Liu, M. H. Zeng, and H. B. Yu, Engineering microdomains of oxides in high-entropy alloy electrodes toward efficient oxygen evolution, *Adv. Mater.* **33**, 2101845 (2021).
- [13] H. D. Li, J. P. Lai, Z. J. Li, and L. Wang, Multi-sites electrocatalysis in high-entropy alloys, *Adv. Funct. Mater.* **31**, 2106715 (2021).
- [14] J. Cavin, A. Ahmadiparidari, L. Majidi, A. S. Thind, S. N. Misal, A. Prajapati, Z. Hemmat, S. Rastegar, A. Beukelman, M. R. Singh, K. A. Unocic, A. Salehi-Khojin, and R. Mishra, 2D high-entropy transition metal dichalcogenides for carbon dioxide electrocatalysis, *Adv. Mater.* **33**, 2100347 (2021).
- [15] P. Xie, Y. Yao, Z. Huang, Z. Liu, J. Zhang, T. Li, G. Wang, R. Shahbazian-Yassar, L. Hu, and C. Wang, Highly efficient decomposition of ammonia using high-entropy alloy catalysts, *Nat. Commun.* **10**, 4011 (2019).
- [16] L. Zhang, W. Cai, and N. Bao, Top-level design strategy to construct an advanced high-entropy Co-Cu-Fe-Mo (oxy)hydroxide electrocatalyst for the oxygen evolution reaction, *Adv. Mater.* **33**, 2100745 (2021).
- [17] H. Zhu, Z. F. Zhu, J. C. Hao, S. H. Sun, S. L. Lu, C. Wang, P. M. Ma, W. F. Dong, and M. L. Du, High-entropy alloy stabilized active Ir for highly efficient acidic oxygen evolution, *Chem. Eng. J. Biochem. Eng. J.* **431**, 133251 (2022).
- [18] Y. J. Mei, Y. B. Feng, C. X. Zhang, Y. Zhang, Q. L. Qi, and J. Hu, High-entropy alloy with mo-coordination as efficient electrocatalyst for oxygen evolution reaction, *ACS Catal.* **12**, 10808 (2022).
- [19] K. Huang, B. W. Zhang, J. S. Wu, T. Y. Zhang, D. Peng, X. Cao, Z. Zhang, Z. Li, and Y. Z. Huang, Exploring the impact of atomic lattice deformation on oxygen evolution reactions based on a sub-5 nm pure face-centred cubic high-entropy alloy electrocatalyst, *J. Mater. Chem. A* **8**, 11938 (2020).
- [20] J. Kwon, S. Sun, S. Choi, K. Lee, S. Jo, K. Park, Y. K. Kim, H. B. Park, H. Y. Park, J. H. Jang, H. Han, U. Paik, and T. Song, Tailored electronic structure of Ir in high entropy alloy for highly active and durable bifunctional electrocatalyst for water splitting under an acidic environment, *Adv. Mater.* **35**, 2300091 (2023).
- [21] Y. F. Ye, Q. Wang, J. Lu, C. T. Liu, and Y. Yang, High-entropy alloy: Challenges and prospects, *Mater. Today* **19**, 349 (2016).
- [22] X. Chang, M. Zeng, K. Liu, and L. Fu, Phase engineering of high-entropy alloys, *Adv. Mater.* **32**, 1907226 (2020).
- [23] A. A. H. Tajuddin, M. Wakisaka, T. Ohto, Y. Yu, H. Fukushima, H. Tanimoto, X. Li, Y. Misu, S. Jeong, J.-i. Fujita, H. Tada, T. Fujita, M. Takeguchi, K. Takano, K. Matsuoka, Y. Sato, and Y. Ito, Corrosion-resistant and high-entropic non-noble-metal electrodes for oxygen evolution in acidic media, *Adv. Mater.* **35**, 2207466 (2023).
- [24] M. W. Glasscott, A. D. Pendergast, S. Goines, A. R. Bishop, A. T. Hoang, C. Renault, and J. E. Dick, Electrosynthesis of high-entropy metallic glass nanoparticles for designer, multi-functional electrocatalysis, *Nat. Commun.* **10**, 2650 (2019).
- [25] Z. Jia, K. Nomoto, Q. Wang, C. Kong, L. Sun, L.-C. Zhang, S.-X. Liang, J. Lu, and J. J. Kruzic, A self-supported high-entropy metallic glass with a nanospunge architecture for efficient hydrogen evolution under alkaline and acidic conditions, *Adv. Funct. Mater.* **31**, 2101586 (2021).
- [26] J. S. Kim, B. Kim, H. Kim, and K. Kang, Recent progress on multimetal oxide catalysts for the oxygen evolution reaction, *Adv. Energy Mater.* **8**, 1702774 (2018).
- [27] J. Tian, Y. Hu, W. Lu, J. Zhu, X. Liu, J. Shen, G. Wang, and J. Schroers, Dealloying of an amorphous TiCuRu alloy results in a nanostructured electrocatalyst for hydrogen evolution reaction, *Carbon Energy* **n/a**, e322 (2023).
- [28] Z. Jin, J. Lyu, Y.-L. Zhao, H. Li, X. Lin, G. Xie, X. Liu, J.-J. Kai, and H.-J. Qiu, Rugged high-entropy alloy nanowires with in situ formed surface spinel oxide as highly stable electrocatalyst in Zn-air batteries, *ACS Mater. Lett.* **2**, 1698 (2020).
- [29] R. Li, R. Wu, Z. Li, J. Wang, X. Liu, Y. Wen, F.-K. Chiang, S.-W. Chen, K. C. Chan, and Z. Lu, Boosting oxygen-evolving activity via atom-stepped interfaces architected with kinetic frustration, *Adv. Mater.* **2206890** (2022).
- [30] Y. Q. Bu, Y. Wu, Z. F. Lei, X. Y. Yuan, H. H. Wu, X. B. Feng, J. B. Liu, J. Ding, Y. Lu, H. T. Wang, Z. P. Lu, and W. Yang, Local chemical fluctuation mediated ductility in body-centered-cubic high-entropy alloys, *Mater. Today* **46**, 28 (2021).
- [31] L. Li, R. D. Kamachali, Z. Li, and Z. F. Zhang, Grain boundary energy effect on grain boundary segregation in an equiatomic high-entropy alloy, *Phys. Rev. Mater.* **4**, 053603 (2020).
- [32] L. Li, Z. Li, A. Kwiatkowski da Silva, Z. R. Peng, H. Zhao, B. Gault, and D. Raabe, Segregation-driven grain boundary spinodal decomposition as a pathway for phase nucleation in a high-entropy alloy, *Acta Mater.* **178**, 1 (2019).
- [33] R. G. Mariano, K. McKelvey, H. S. White, and M. W. Kanan, Selective increase in CO₂ electroreduction activity at grain-boundary surface terminations, *Science* **358**, 1187 (2017).
- [34] Y. Chen, C. W. Li, and M. W. Kanan, Aqueous CO₂ reduction at very low overpotential on oxide-derived Au nanoparticles, *J. Am. Chem. Soc.* **134**, 19969 (2012).
- [35] X. Feng, K. Jiang, S. Fan, and M. W. Kanan, Grain-boundary-dependent CO₂ electroreduction activity, *J. Am. Chem. Soc.* **137**, 4606 (2015).
- [36] C. Hu and J. Luo, Data-driven prediction of grain boundary segregation and disordering in high-entropy alloys in a 5D space, *Mater. Horiz.* **9**, 1023 (2022).
- [37] J. Wang, P. Jiang, F. Yuan, and X. Wu, Chemical medium-range order in a medium-entropy alloy, *Nat. Commun.* **13**, 1021 (2022).
- [38] Z. J. Gu, Y. Z. Tian, W. Xu, S. Lu, X. L. Shang, J. W. Wang, and G. W. Qin, Optimizing transformation-induced plasticity in CoCrNi alloys by combined grain refinement and chemical tuning, *Scr. Mater.* **214**, 114658 (2022).
- [39] X. W. Liu, L. Liu, G. Liu, X. X. Wu, D. H. Lu, J. Q. Yao, W. M. Jiang, Z. T. Fan, and W. B. Zhang, The role of carbon in grain refinement of cast CrFeCoNi high-entropy alloys,

- Metall. Mater. Trans. A: Phys. Metall. Mater. Sci. **49**, 2151 (2018).
- [40] See Supplemental Material at <http://link.aps.org/supplemental/10.1103/PRXEnergy.2.033011> for details of the experimental methods, structural information of the samples, OER performances, TEM characterization of grain boundaries of activated catalysts, ICP-OES results of electrolyte solutions after OER, and XPS results.
- [41] G. Laplanche, A. Kostka, C. Reinhart, J. Hunfeld, G. Eggeler, and E. P. George, Reasons for the superior mechanical properties of medium-entropy CrCoNi compared to high-entropy CrMnFeCoNi, *Acta Mater.* **128**, 292 (2017).
- [42] S. Abhaya, R. Rajaraman, S. Kalavathi, and G. Amarendra, Positron annihilation studies on FeCrCoNi high entropy alloy, *J. Alloys Compd.* **620**, 277 (2015).
- [43] Z. Fang, P. Wu, Y. Qian, and G. Yu, Gel-derived amorphous bismuth–nickel alloy promotes electrocatalytic nitrogen fixation via optimizing nitrogen adsorption and activation, *Angew. Chem., Int. Ed.* **60**, 4275 (2021).
- [44] S. Gao, S. Hao, Z. Huang, Y. Yuan, S. Han, L. Lei, X. Zhang, R. Shahbazian-Yassar, and J. Lu, Synthesis of high-entropy alloy nanoparticles on supports by the fast moving bed pyrolysis, *Nat. Commun.* **11**, 2016 (2020).
- [45] H. K. Park, H. Ahn, T. H. Lee, J. Y. Lee, M. G. Lee, S. A. Lee, J. W. Yang, S. J. Kim, S. H. Ahn, S. Y. Kim, C. H. Lee, E. S. Park, and H. W. Jang, Grain boundaries boost oxygen evolution reaction in NiFe electrocatalysts, *Small Methods* **5**, e2000755 (2021).
- [46] S. W. Im, H. Ahn, E. S. Park, K. T. Nam, and S. Y. Lim, Electrochemically activated NiFeO_xH_y for enhanced oxygen evolution, *ACS Appl. Energy Mater.* **4**, 595 (2021).
- [47] Y. C. Hu, Y. Z. Wang, R. Su, C. R. Cao, F. Li, C. W. Sun, Y. Yang, P. F. Guan, D. W. Ding, Z. L. Wang, and W. H. Wang, A highly efficient and self-stabilizing metallic-glass catalyst for electrochemical hydrogen generation, *Adv. Mater.* **28**, 10293 (2016).
- [48] Y.-C. Hu, C. Sun, and C. Sun, Functional applications of metallic glasses in electrocatalysis, *ChemCatChem* **11**, 2401 (2019).
- [49] N. Li, R. G. Hadt, D. Hayes, L. X. Chen, and D. G. Nocera, Detection of high-valent iron species in alloyed oxidic cobaltates for catalysing the oxygen evolution reaction, *Nat. Commun.* **12**, 4218 (2021).
- [50] H. J. Qiu, G. Fang, J. Gao, Y. R. Wen, J. Lv, H. L. Li, G. Q. Xie, X. J. Liu, and S. H. Sun, Noble metal-free nanoporous high-entropy alloys as highly efficient electrocatalysts for oxygen evolution reaction, *ACS Mater. Lett.* **1**, 526 (2019).
- [51] Z. Y. Ding, J. Bian, S. Shuang, X. D. Liu, Y. C. Hu, C. W. Sun, and Y. Yang, High entropy intermetallic-oxide core-shell nanostructure as superb oxygen evolution reaction catalyst, *Adv. Sustain. Syst.* **4**, 1900105 (2020).
- [52] Y. Tong, J. Wu, P. Chen, H. Liu, W. Chu, C. Wu, and Y. Xie, Vibronic superexchange in double perovskite electrocatalyst for efficient electrocatalytic oxygen evolution, *J. Am. Chem. Soc.* **140**, 11165 (2018).
- [53] Y. Li, Z. S. Wu, P. Lu, X. Wang, W. Liu, Z. Liu, J. Ma, W. Ren, Z. Jiang, and X. Bao, High-valence nickel single-atom catalysts coordinated to oxygen sites for extraordinarily activating oxygen evolution reaction, *Adv. Sci.* **7**, 1903089 (2020).
- [54] H. B. Tao, Y. Xu, X. Huang, J. Chen, L. Pei, J. Zhang, J. G. Chen, and B. Liu, A general method to probe oxygen evolution intermediates at operating conditions, *Joule* **3**, 1498 (2019).
- [55] I. A. Cechanaviciute, R. P. Antony, O. A. Krysiak, T. Quast, S. Dieckhofer, S. Saddeler, P. Telaar, Y. T. Chen, M. Mueller, and W. Schuhmann, Scalable synthesis of multi-metal electrocatalyst powders and electrodes and their application for oxygen evolution and water splitting, *Angew. Chem. Int. Ed.* **62**, e202218493 (2023).
- [56] O. Diaz-Morales, D. Ferrus-Suspèdra, and M. T. M. Koper, The importance of nickel oxyhydroxide deprotonation on its activity towards electrochemical water oxidation, *Chem. Sci.* **7**, 2639 (2016).
- [57] A. C. Garcia, T. Touzalin, C. Nieuwland, N. Perini, and M. T. M. Koper, Enhancement of oxygen evolution activity of nickel oxyhydroxide by electrolyte alkali cations, *Angew. Chem., Int. Ed.* **58**, 12999 (2019).
- [58] C. Hu, Y. Hu, C. Fan, L. Yang, Y. Zhang, H. Li, and W. Xie, Surface-enhanced Raman spectroscopic evidence of key intermediate species and role of NiFe dual-catalytic center in water oxidation, *Angew. Chem., Int. Ed.* **60**, 19774 (2021).
- [59] H. Y. Wang, S. F. Hung, Y. Y. Hsu, L. Zhang, J. Miao, T. S. Chan, Q. Xiong, and B. Liu, In situ spectroscopic identification of μ -OO bridging on spinel Co_3O_4 water oxidation electrocatalyst, *J. Phys. Chem. Lett.* **7**, 4847 (2016).
- [60] J. Kadrman and J. Cadek, The energy of coherent twin boundaries of some metals and alloys, *Philos. Mag.* **20**, 413 (1969).
- [61] Q. Pan, L. Zhang, R. Feng, Q. Lu, K. An, A. C. Chuang, J. D. Poplawsky, P. K. Liaw, and L. Lu, Gradient cell-structured high-entropy alloy with exceptional strength and ductility, *Science* **374**, 984 (2021).